

# POLITECNICO MILANO 1863

Spacecraft Attitude Dynamics

Academic Year 2025/2026

**Project group n.: 30**

**Project n.: 566**

**Team members:**

*This table is mandatory*

Person code	Surname	Name	Bachelor (type and University)
	Isernia	Federico	Mechanical Engineering - PoliMi
	Mazza	Alberto	Aerospace Engineering - PoliMi
	Cicchetti	Mattia	Aerospace Engineering - UniPd
	<b>Caccia</b>	<b>Riccardo</b>	Aerospace Engineering - PoliMi

Prof: F. Bernelli Zazzera  
Prof: A. Colagrossi

**Project specifications:***This table is mandatory*

	<b>Assigned specification</b>	<b>Modifications (if any)</b>	<b>Motivation for modification</b>
<b>Platform</b>	minisat(100-500 kg)	-	-
<b>Attitude parameters</b>	Direction cosines		
<b>Mandatory sensor</b>	Star sensor	Magnetometer	Needed for Magnetorquers and Detumbling
<b>Actuators</b>	3 magnetic coils, 1 reaction wheel		

**Team members work distribution (if applicable):**

<b>Surname</b>	<b>Name</b>	<b>Specific role in project</b>

# Contents

<b>1</b>	<b>Introduction</b>	<b>1</b>
1.1	Design Philosophy and Verification Strategy . . . . .	1
1.2	Mission Scenario and Requirements . . . . .	1
1.3	Spacecraft Structure . . . . .	2
1.4	Orbit Specifications . . . . .	3
<b>2</b>	<b>Dynamics</b>	<b>3</b>
2.1	Validation . . . . .	4
<b>3</b>	<b>Kinematics</b>	<b>5</b>
3.1	Validation . . . . .	5
<b>4</b>	<b>Environment &amp; Disturbances</b>	<b>6</b>
4.1	Earth Magnetic Field Model . . . . .	6
4.2	Magnetic Torque . . . . .	7
4.3	Gravity Gradient . . . . .	7
<b>5</b>	<b>Sensors</b>	<b>8</b>
5.1	Magnetometer . . . . .	8
5.2	Star Sensor . . . . .	9
<b>6</b>	<b>Attitude Determination</b>	<b>11</b>
6.1	Static Attitude Determination . . . . .	11
6.2	Dynamic Attitude Determination . . . . .	12
<b>7</b>	<b>Controller Design</b>	<b>13</b>
7.1	Pointing Control . . . . .	14
<b>8</b>	<b>Actuators</b>	<b>16</b>
<b>9</b>	<b>Simulation Results and Performance Analysis</b>	<b>17</b>
9.1	Attitude Determination & Control Performance . . . . .	17
9.2	Actuator Feasibility and Saturation Analysis . . . . .	20
	<b>Bibliography</b>	<b>21</b>

# 1 Introduction

## 1.1 Design Philosophy and Verification Strategy

The development workflow of the Attitude Determination and Control System (ADCS) adhered to the **V-Model** systems engineering framework. This methodological approach was explicitly selected to prioritize the rigorous *Verification and Validation* (V&V) of each system component prior to full integration.

Consistent with the V-Model principles, the implementation phase followed a strict bottom-up validation strategy: each functional module, ranging from the Disturbances to the specific control laws, was individually isolated and validated against its design requirements. Only after confirming the performance of these individual units was the complete closed-loop system assembled. This "component-first" philosophy ensures that potential modeling errors or instabilities are identified and resolved at the unit level, preventing fault propagation and guaranteeing the robustness of the final integrated simulation.

## 1.2 Mission Scenario and Requirements

**Scientific Context** The mission profile is defined within the framework of rapid-response multi-messenger astronomy. The Laser Interferometer Gravitational-Wave Observatory (LIGO) has recently detected an anomalous burst of gravitational waves, cataloged as event *GW-251225*. Preliminary data analysis suggests that this signal originates from a Tidal Disruption Event (TDE), designated as **Fenrir-X1**. To characterize the electromagnetic counterpart of this transient event, a Low Earth Orbit (LEO) satellite is deployed. The satellite payload consists of a **Wide-Field Optical Imager** designed to capture the light curve of the target star. For simulation and design purposes, the target is defined to be aligned with the principal inertial axis ( $\mathbf{A}_{target} = \mathbf{I}_{3\times 3}$ ).

**Design Constraints and Requirements** This project is developed under specific hardware constraints typical of low-cost academic or technology demonstrator missions. The most critical constraint is the absence of inertial rate gyroscopes. Consequently, the angular rates required for the damping control laws must be reconstructed entirely via the estimation filter (MEKF), relying on attitude updates from the Star Sensor and Magnetometer.

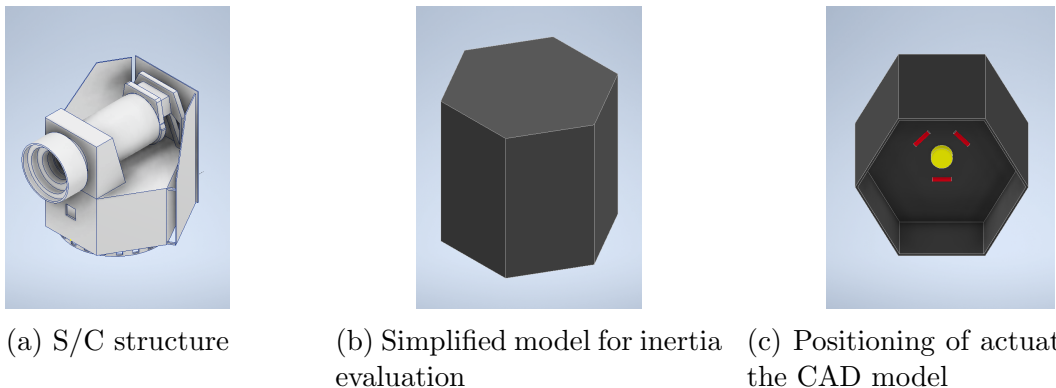
Acknowledging this "gyro-less" architecture and the resulting challenges in estimating high-frequency dynamics, the performance requirements have been defined with appropriate margins to ensure robustness:

- **Absolute Pointing Error (APE):** The system is required to maintain an absolute pointing accuracy better than **5 degree** ( $3\sigma$ ). This metric, defined as the instantaneous angular separation between the estimated body axis and the target vector, ensures that the target star remains essentially centered within the payload field of view.
- **Relative Pointing Error (RPE) / Stability:** To prevent image smearing during the exposure time, the satellite must exhibit high pointing stability. The RPE represents the variation of the pointing error over a specific integration time window. For this mission, a stability requirement of **0.05 deg/s** ( $3\sigma$ ) is defined to ensure sharp image acquisition.

- **Attitude Determination Accuracy:** The determination subsystem is required to estimate the satellite's attitude with an error lower than **1 degree**. While the on-board Star Tracker is capable of higher precision, this conservative requirement accounts for the potential degradation in the filter's performance due to the lack of direct angular rate measurements.
- **Detumbling Time:** The attitude control system is required to autonomously stabilize the spacecraft from the initial tumbling state within **3 orbital periods**. Specifically, the detumbling phase is considered complete when the norm of the angular velocity vector drops below the safety threshold of  $\|\omega\| \leq 0.05 \text{ rad/s}$ , allowing for the subsequent activation of the reaction wheel and starting the pointing phase.

### 1.3 Spacecraft Structure

Since the requested is a minisat between 100 and 500 kg, it has been decided to select an existing to use as a model for the comprehension of the structure and dimensions and the calculation of real inertia values. The selection fell on CHEOPS, a minisat by ESA, whose CAD model can be seen in Fig.1a. The weight is 290kg and include, as instruments, between others, also magnetorquers and reaction [3]. In the CAD model has been decided to represent only the actuators requested in the project, represented in Fig.1c. The reaction wheel is depicted in yellow, while the three magnetorquers are depicted in red. To retrieve the inertia values along the three axis, a very simplified CAD model of the satellite has been created, represented in Fig.1b, neglecting almost all elements and keeping only the principal shape, to be able to guarantee the symmetry, otherwise very difficult to achieve since the exact configuration of the is not available.



The calculated values of inertia can bee seen in 1, given in  $\frac{\text{kg}}{\text{m}^2}$ . They are coherent with inertia values for other similar satellites in terms of dimensions and weight.

Table 1: Inertia Moments along the three axes

Parameter	Value [ $\text{kg}\cdot\text{m}^2$ ]
X Axis ( $I_{xx}$ )	62.46
Y Axis ( $I_{yy}$ )	81.04
Z Axis ( $I_{zz}$ )	62.45

## 1.4 Orbit Specifications

The selection of the orbital parameters is a critical step in the ADCS design process, as the orbital environment directly dictates the magnitude of external disturbance torques and the availability of control authority, particularly for magnetic actuation. The simulation scenario is defined by the Keplerian parameters listed in Table 2.

The chosen orbit is a **Low Earth Orbit (LEO)**. This regime is optimal for missions relying on magnetic control, as the Earth's magnetic field strength decays with the cube of the distance. In LEO, the magnetic field intensity is sufficient to generate adequate control torque using magnetorquers within reasonable power and size constraints.

A **non-zero Inclination ( $i$ )** (specifically, an inclined orbit rather than an equatorial one) was selected as a mandatory requirement for three-axis magnetic stabilization. In an equatorial orbit, the geomagnetic field vector remains predominantly perpendicular to the equatorial plane, creating a permanent geometric singularity where torque cannot be generated around the local magnetic field line. By selecting an inclined orbit, the satellite sweeps through varying magnetic latitudes, ensuring that the magnetic field vector rotates significantly within the body frame over the course of an orbit. This variation is fundamental to guarantee average controllability on all three axes using the B-Dot and magnetic damping laws.

Furthermore, a **slight eccentricity ( $e$ )** has been introduced in the simulation model. While nominal mission operations often target circular orbits, a quasi-circular orbit with small eccentricity allows for the validation of the controller's robustness. This variation introduces fluctuations in altitude, thereby subjecting the control system to varying environmental disturbances (e.g., atmospheric density changes and gravity gradient oscillations) and magnetic field intensities, proving the system's capability to handle realistic orbital insertion errors.

Finally, the Right Ascension of the Ascending Node ( $\Omega$ ) and the Argument of Perigee ( $\omega$ ) were initialized to zero. These parameters define the orientation of the orbit in inertial space at the epoch and do not inherently affect the dynamic performance of the attitude control logic relative to the local orbital frame.

Table 2: Selected Orbital Parameters for ADCS Simulation

Parameter	Value
Semi-major Axis ( $a$ )	6878 km
Eccentricity ( $e$ )	0.2
Inclination ( $i$ )	40 deg
RAAN ( $\Omega$ )	0 deg
Argument of Perigee ( $\omega$ )	0 deg
True Anomaly ( $\Theta_0$ )	0 deg

## 2 Dynamics

The implemented dynamics model is based on Euler's equations:

$$\mathbf{J} \dot{\boldsymbol{\omega}} + \boldsymbol{\omega} \times (\mathbf{J} \boldsymbol{\omega}) = \mathbf{0}, \quad (1)$$

where  $\mathbf{J} = \text{diag}(I_1, I_2, I_3)$  represents the spacecraft inertia matrix and  $\boldsymbol{\omega}$  its angular velocity expressed in the body frame.

## 2.1 Validation

The torque-free rotational dynamics of the spacecraft were validated by verifying the conservation of the angular momentum  $H$  and the kinetic energy  $K$ , as well as the qualitative stability behavior associated with the principal inertia axes.

In the absence of external torques, the angular momentum magnitude  $H = \|\mathbf{J}\boldsymbol{\omega}\|$  and the rotational kinetic energy  $K = \frac{1}{2}\boldsymbol{\omega}^T \mathbf{J} \boldsymbol{\omega}$  must remain constant over time.

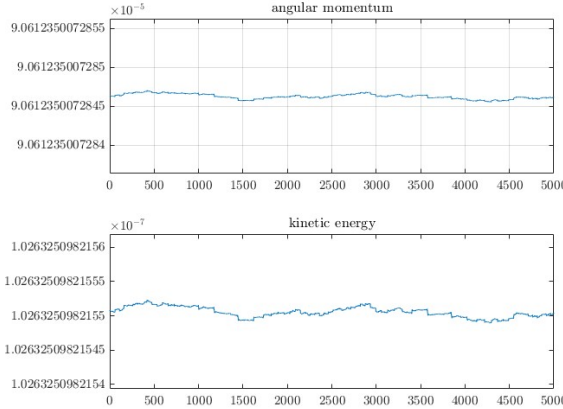


Figure 2: Angular Momentum  $H$  and Kinetic Energy  $K$  conservation

Figure 2 shows that both quantities are conserved within numerical precision, confirming the correct implementation of Euler's equations.

To further assess the stability properties, simulations were performed for small perturbations of the angular velocity about each principal axis of inertia. When the spacecraft spins about the maximum or minimum inertia axis, the motion remains stable and the angular velocity components oscillate periodically. Conversely, when the spin occurs about the intermediate inertia axis, the solution becomes unstable and the angular velocity exhibits growing oscillations, as shown in Figure 3.

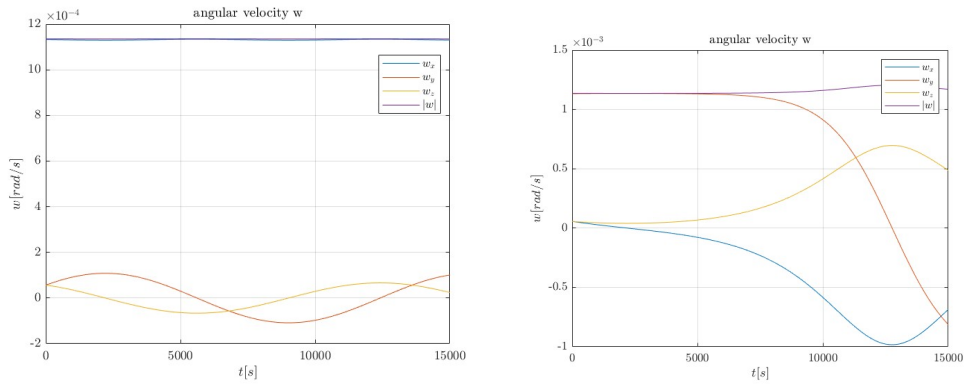


Figure 3: spacecraft response to small perturbations orthogonal to spin axis

These results confirm that the implemented model reproduces the expected physical behavior of torque-free rigid-body dynamics.

### 3 Kinematics

The attitude kinematics are governed by the differential equation

$$\dot{\mathbf{A}}_{BN} = \mathbf{A}_{BN} [\boldsymbol{\omega}_B]^\wedge, \quad (2)$$

where  $\mathbf{A}_{BN}$  represents the rotation matrix from the inertial to the body frame, and  $[\boldsymbol{\omega}_B]^\wedge$  is the skew-symmetric matrix associated with the angular velocity vector  $\boldsymbol{\omega}_B$ .

#### 3.1 Validation

The kinematic model was validated by verifying the numerical consistency of the Direction Cosine Matrix (DCM) definition.

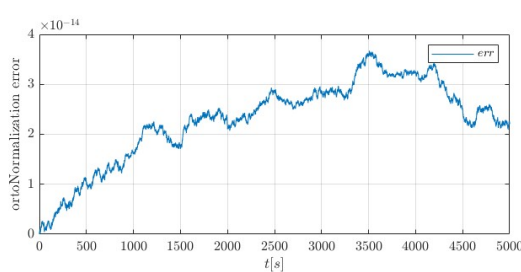
To mitigate the accumulation of numerical drift due to integration, an orthonormalization step was implemented using the symmetric form

$$\mathbf{A}_{new} = \frac{3}{2} \mathbf{A} - \frac{1}{2} \mathbf{A} (\mathbf{A}^\top \mathbf{A}), \quad (3)$$

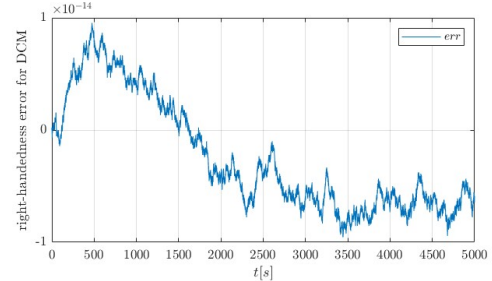
which restores the orthogonality of  $\mathbf{A}_{BN}$  without altering its physical orientation. However, to reduce the computational cost, this correction is not applied at every integration step: it is activated only when the orthonormalization error exceeds a predefined threshold, ensuring a balance between numerical accuracy and computational efficiency.

The validation was performed by monitoring two key quantities during a torque-free simulation:

- the *orthonormalization error*, defined as  $\|\mathbf{A}_{BN} \mathbf{A}_{BN}^\top - \mathbf{I}\|$ , which quantifies the deviation from orthogonality;
- the *right-handedness error*, computed as  $\det(\mathbf{A}_{BN}) - 1$ , which verifies the preservation of the DCM handedness.



(a) orthonormalization error for DCM



(b) right-handedness error for DCM

Figure 4: DCM definition errors

Both errors remained below  $10^{-13}$  throughout the simulation, as shown in Figure 4, demonstrating the numerical stability and accuracy of the implemented kinematic integration and normalization algorithm.

## 4 Environment & Disturbances

In compliance with the project specifications, the simulation environment was required to account for the two most significant environmental perturbations. Following a preliminary order-of-magnitude analysis, the Gravity Gradient and the Residual Magnetic Dipole torque were identified as the dominant disturbance sources for the selected orbital regime and were consequently implemented in the dynamic model.

### 4.1 Earth Magnetic Field Model

**Validation** The Earth magnetic field model was validated through a sequence of analytical and numerical tests aimed at verifying both the correctness of the dipole formulation and its Simulink implementation. In the initial analyses, the geomagnetic dipole was assumed to be aligned with the vertical axis of the inertial frame, which simplifies the validation and makes the expected field directions immediately recognizable.

Static configurations were first examined by fixing the spacecraft position along specific directions. The model correctly produced a purely vertical field at the magnetic poles and a purely horizontal field at the magnetic equator, consistent with the expected behaviour of a vertically aligned dipole.

Finally, the model was tested along a representative polar orbit. The temporal evolution of the magnetic field components exhibited the characteristic double-frequency modulation associated with a dipole observed along a polar trajectory. Vertical markers were added to highlight equator crossings and pole passages, which aligned with the extrema of the orbital  $z$ -coordinate, further confirming the temporal and geometric consistency of the model.

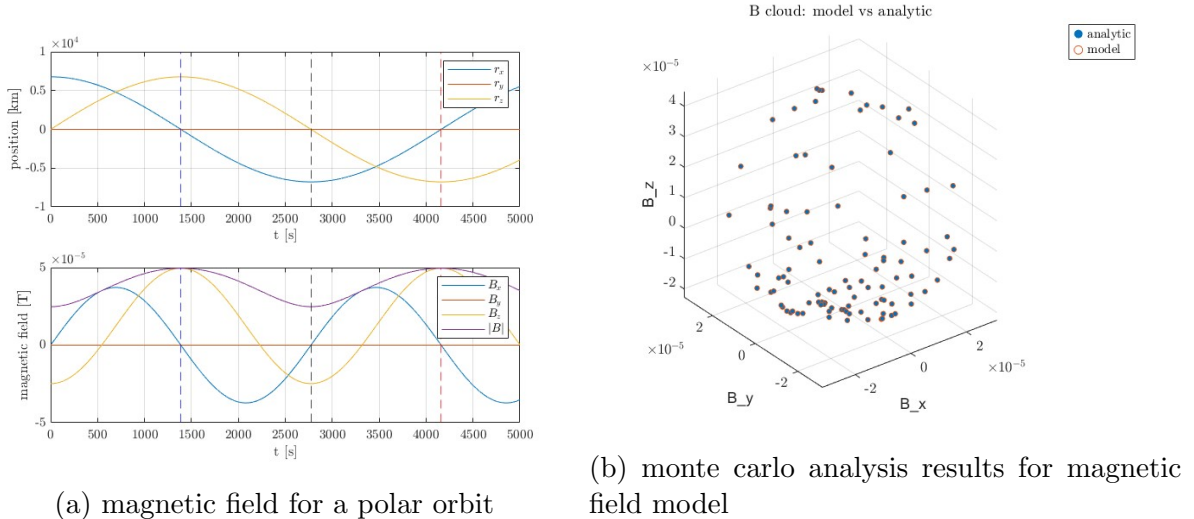


Figure 5: magnetic field model validation

A second validation step assessed the geometric consistency of the field direction using a Monte Carlo comparison between the analytical dipole equation and the Simulink output for a set of randomly generated position vectors. The resulting clouds overlapped almost perfectly, confirming the correct computation of the dipole term  $3(\hat{m} \cdot \hat{r})\hat{r}$  and its transformation to the inertial frame.

Overall, the tests demonstrate that the implemented magnetic field model accurately reproduces the direction, magnitude, and spatial variation of the first-order geomagnetic dipole field and is therefore suitable for use in the magnetic disturbance torque model.

## 4.2 Magnetic Torque

the magnetic disturbance torque implementation was verified. The adopted model is the standard dipole relation

$$\boldsymbol{\tau}_m = \mathbf{j}_B \times \mathbf{b}_B,$$

where  $\mathbf{j}_B$  is the spacecraft residual magnetic dipole expressed in the body frame and  $\mathbf{b}_B$  is the geomagnetic field in body axes.

**Validation** Since the torque expression is a direct cross product between two already validated vectors, only a set of simple consistency checks was deemed necessary. Static test cases were performed by selecting parallel and orthogonal configurations of  $\mathbf{j}_B$  and  $\mathbf{b}_B$ . When the two vectors were aligned, the resulting torque was numerically zero, whereas for orthogonal configurations the torque direction matched the right-hand rule and its magnitude was consistent with  $\|\boldsymbol{\tau}_m\| = \|\mathbf{j}_B\| \|\mathbf{b}_B\| \sin \theta$ . A further dynamic test along a polar orbit confirmed that the time evolution of the magnetic torque is coherent with that of the magnetic field and remains orthogonal to  $\mathbf{b}_B$  at all times.

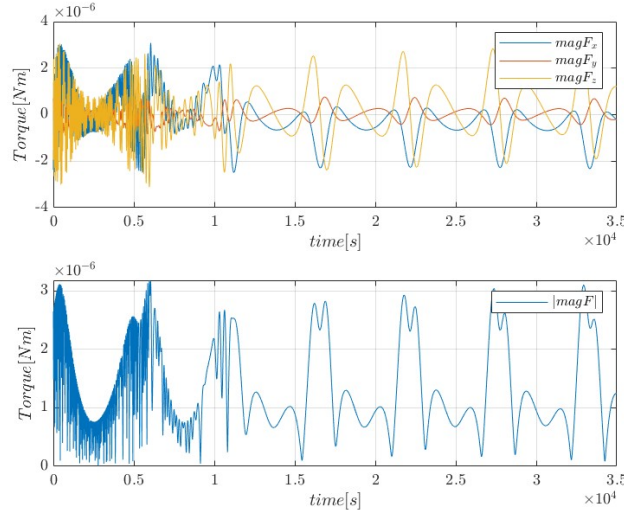


Figure 6: Magnetic Torque Perturbation

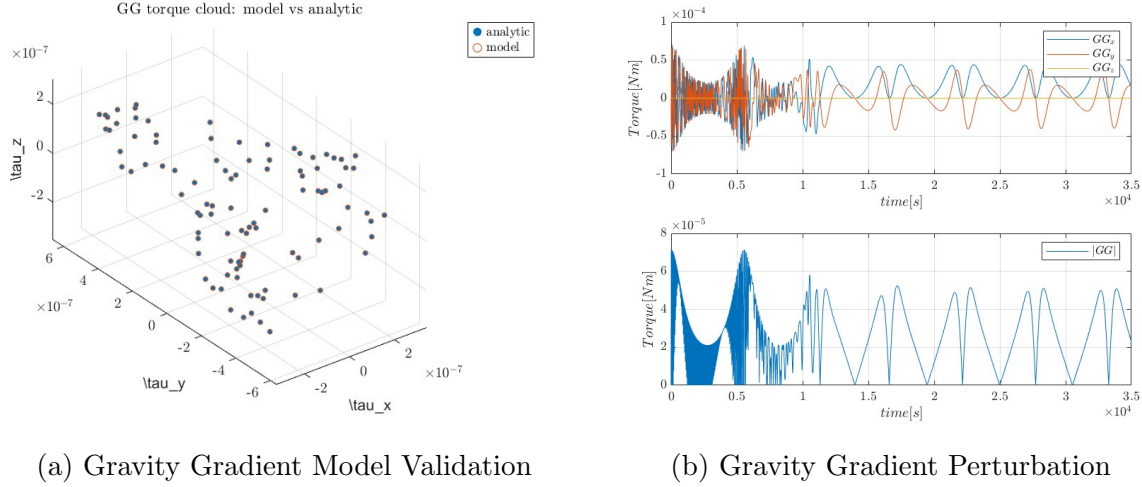
Final result of total Magnetic Torque Perturbation actioning on the spacecraft is proposed here in Figure 6

## 4.3 Gravity Gradient

**Validation** To verify the correct implementation of the gravity-gradient torque model, a set of static configurations was simulated by fixing the Nadir direction  $\hat{\mathbf{r}}$  in the body frame.

Tests were performed for Nadir directions halfway between pairs of principal inertia axes, corresponding to  $\hat{\mathbf{r}} = [1, 1, 0]/\sqrt{2}$ ,  $[1, 0, 1]/\sqrt{2}$ , and  $[0, 1, 1]/\sqrt{2}$ .

The simulated results matched both the direction and magnitude predicted analytically: for each case, the torque vector was orthogonal to the plane defined by  $\hat{\mathbf{r}}$  and the corresponding principal inertia axes, as expected from the cross-product nature of the model. Furthermore, when  $\hat{\mathbf{r}}$  was aligned with one of the principal inertia axes, the torque correctly vanished within numerical precision. These results confirm the correctness of the gravity-gradient torque implementation in both magnitude and orientation.



A Monte Carlo comparison between the analytical gravity-gradient torque expression and the Simulink implementation was performed over 200 random Nadir directions in the body frame. The torque vectors obtained from the model (orange markers) perfectly overlap with the analytical reference (blue markers), confirming the correctness of both direction and magnitude of the implemented formulation. The relative error was found to be below  $1e-7$ , and the orthogonality condition was satisfied within numerical precision. These results validate the gravity-gradient torque model across the entire orientation domain.

## 5 Sensors

### 5.1 Magnetometer

**Modelling** The magnetometer implemented in the simulation is based on a standard error model typically adopted for CubeSat-class sensors. The measured magnetic field vector  $\mathbf{b}_{\text{meas}}$  is obtained by applying a sequence of deterministic and stochastic error sources to the true magnetic field  $\mathbf{b}_{\text{true}}$ . The model includes a small misalignment between the sensor axes and the body frame, represented by the matrix  $\mathbf{M}_{\text{mis}}$ , as well as a non-orthogonality matrix  $\mathbf{M}_{\text{orth}}$  which accounts for the fact that the three sensing axes are not perfectly orthogonal. Linear scale factor errors, scale factor asymmetry and scale factor nonlinearity are included through three separate terms that modify the measured field component-wise. After these systematic effects, the model adds a slowly varying bias term and a stochastic noise component composed of white noise, pink noise, and a random-walk contribution.

**Error Characterisation** Figure 8a shows the time history of the measurement error  $\mathbf{e}(t) = \mathbf{b}_{\text{meas}}(t) - \mathbf{b}_{\text{true}}(t)$ . The error evolves in a manner fully consistent with the sensor

model described above. High-frequency fluctuations are primarily determined by the white-noise component, while gradual variations originate from the combined effect of scale-factor errors, misalignment and non-orthogonality. The long-term drift visible in the error is a consequence of the bias instability introduced through the random-walk term in the noise model. It is also worth noting that a constant bias does not appear explicitly in the Allan deviation, as the Allan statistic inherently removes any static offset by differencing consecutive averages.

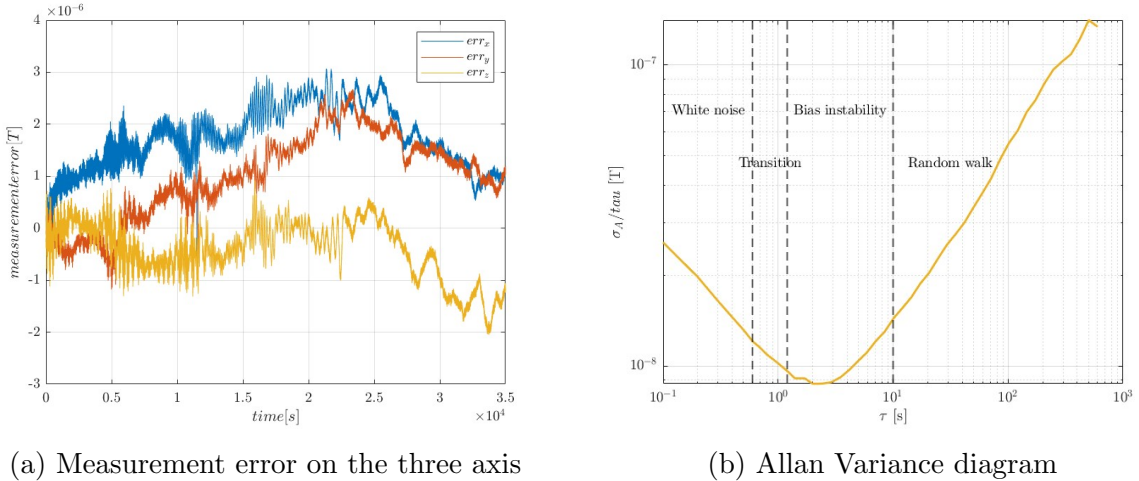


Figure 8: Magnetometer measurement error analysis

The Allan deviation of the magnetometer error was computed in order to characterise the sensor’s noise behaviour as a function of the averaging time  $\tau$ . The resulting plot, shown in Fig. 8b, exhibits the expected “U-shaped” profile. For short averaging times, the Allan deviation decreases with a slope close to  $-1/2$ , indicating that the measurement is dominated by white noise. As  $\tau$  increases, the curve reaches a minimum corresponding to the transition region, which identifies an optimal averaging time where the trade-off between white noise and drift is most favourable. For larger values of  $\tau$ , the Allan deviation increases with a slope approaching  $+1/2$ , revealing the presence of bias instability and random-walk effects. This behaviour confirms that the simulated magnetometer reproduces the characteristic noise processes observed in real sensors of comparable class.

## 5.2 Star Sensor

**Modelling** The star sensor has been modelled by reproducing, as closely as possible, the sequence of operations performed by a real optical star tracker. The objective of this star sensor model is to provide the attitude determination algorithm with a set of reliable unit vectors corresponding to the directions of the brightest stars inside the instrument field of view.

The starting point was the *Bright Star Catalogue*, which contains the equatorial coordinates and visual magnitudes of all stars brighter than magnitude 6.5, that is, roughly speaking, all the stars visible to the naked eye from Earth. Since a spacecraft-mounted star tracker typically detects stars up to approximately sixth magnitude, all entries with visual magnitude greater than this threshold were removed in order to reduce the size of the catalogue while preserving all observable celestial sources.

After conversion of *Right Ascension* and *Declination* parameters, each star direction was represented in the inertial reference frame by a unit vector, giving finally a clean inertial star catalogue consisting of approximately four thousand stars, each represented by a normalised three-dimensional vector.

At each simulation step, the star sensor receives the current spacecraft attitude expressed by the direction cosine matrix from the body frame to the inertial frame. This matrix is used to transform all catalogue vectors from the inertial frame into the body frame and then into the sensor frame through a fixed misalignment rotation that accounts for possible mechanical installation imperfections. The sensor then evaluates, for each catalogue star, the angular separation between its direction and the *boresight axis*. Only the stars lying within the instrument field of view (60) are considered observable and among these, the four brightest are selected in order to guarantee both redundancy and robustness in the subsequent attitude estimation stage. This choice reflects the behaviour of many flight-qualified star trackers, which typically provide a list of the most "reliable" stars rather than the full set of all visible stars.

The sensor measurements are then normalised and passed to the measurement error model, which adds angular perturbations and noise consistent with the performance values reported in the manufacturer documentation, including the specified pointing accuracy and update rate.

To accurately emulate hardware timing, the model operates at a distinct sampling rate (5 Hz) decoupled from the high-frequency spacecraft dynamics. A rate transition block downsamples the input attitude, triggering the star-mapping process only at the sensor update rate. A second block acts as a Zero-Order Hold on the output, ensuring the GNC algorithm receives the most recent valid measurement at every integration step.

**Error Characterisation** In this work the star tracker is not used in its full attitude-determination configuration, but rather as a vector-mode sensor providing a set of stellar directions expressed in the spacecraft body frame. The attitude estimation is performed separately through static and dynamic algorithms, and therefore the star sensor model is limited to the generation of noisy line-of-sight measurements for a set of catalog stars.

The dominant source of uncertainty in a star tracker operating in vector-mode is the angular measurement error, which primarily originates from centroiding uncertainty on the image plane. Such error is well modelled as a small random rotation orthogonal to the measured direction. Denoting by  $\delta\boldsymbol{\theta}_i$  a small rotation vector with zero mean and standard deviation consistent with the star tracker accuracy (e.g., 10 arcsec at  $1\sigma$ ), the noisy measurement in the sensor frame is

$$\mathbf{s}_{i,\text{meas}}^S = \mathbf{s}_i^S + \delta\boldsymbol{\theta}_i \times \mathbf{s}_i^S, \quad \|\delta\boldsymbol{\theta}_i\| \sim \mathcal{N}(0, \sigma_\theta^2).$$

The resulting vector is finally normalised. Since the attitude determination algorithm requires all measurements to be expressed in the spacecraft body frame, the noisy sensor-frame measurement is mapped back into the body frame through the inverse of the misalignment matrix.

The resulting  $\mathbf{s}_{i,\text{meas}}^B$  represents the simulated star tracker output used by the attitude determination algorithm. This model captures the key error mechanisms relevant for vector-based attitude estimation, while avoiding unnecessary complexity such as scale factor, bias drift, quantisation, or Allan-variance effects, which are not representative of optical sensors.

**Hardware Selection** The sensor selection process is based on the technical specifications provided by the manufacturers for the Mini-Satellite class, specifically the *ST 200* star sensor [1] and the *NewSpace Systems* magnetometer [5].

Sensor Type	Selected Model	Key Characteristics
Star Tracker (x1)	ST 200	<ul style="list-style-type: none"> <li>• Accuracy(<math>3\sigma</math>): 30 arcsec (out)</li> <li>• Accuracy(<math>3\sigma</math>): 200 arcsec (in)</li> <li>• Update Rate: 5 Hz</li> <li>• Field of View: 60° (Circular)</li> </ul>
Magnetometer (x1)	NewSpace Systems	<ul style="list-style-type: none"> <li>• Type: 3-Axis Fluxgate</li> <li>• Range: <math>\pm 60,000</math> nT</li> <li>• Resolution: 7.324 nT</li> <li>• Orthogonality: <math>&lt; \pm 1^\circ</math></li> <li>• Noise Density: <math>&lt; 500</math> pT/<math>\sqrt{\text{Hz}}</math></li> </ul>

Table 3: Sensor Hardware Selection and Specifications

## 6 Attitude Determination

### 6.1 Static Attitude Determination

Static attitude determination aims to estimate the spacecraft orientation at a single instant using only vector measurements. In this project, the estimation is performed through the *q*-method, an analytic solution to Wahba's problem that provides the optimal attitude quaternion from a set of body-frame observations and their corresponding inertial-frame reference vectors.

Given  $N$  pairs of vectors  $(\mathbf{s}_i, \mathbf{v}_i)$  with associated weights  $a_i$ , Wahba's problem consists in minimizing the loss function

$$J(\mathbf{A}) = \frac{1}{2} \sum_{i=1}^N a_i \|\mathbf{s}_i - \mathbf{A}_{B/N} \mathbf{v}_i\|^2, \quad (4)$$

The *q*-method reformulates the maximization in quaternion form by constructing the  $4 \times 4$  Davenport matrix

$$\mathbf{K} = \begin{bmatrix} \mathbf{S} - \sigma \mathbf{I}_3 & \mathbf{z} \\ \mathbf{z}^\top & \sigma \end{bmatrix}, \quad (5)$$

obtaining so, the optimal attitude quaternion as the eigenvector of  $\mathbf{K}$  associated with its largest eigenvalue. [4]

In this specific implementation, the static attitude is determined using exclusively the four star vectors provided by the Star Sensor. The magnetometer data is intentionally discarded from this stage, since the *q*-method minimizes a loss function weighted by sensor precision and so the contribution of the magnetic vector would be orders of magnitude less accurate than the Star Tracker one and statistically negligible. However, being a memoryless static solution, this method cannot estimate the spacecraft's angular rates or gyro biases. Consequently, a Multiplicative Extended Kalman Filter (MEKF) is adopted to fully recover the rotational dynamics.

## 6.2 Dynamic Attitude Determination

The navigation solution relies on a Multiplicative Extended Kalman Filter (MEKF). This architecture is specifically selected to address two primary objectives: reconstructing the angular rates  $\omega$  in a gyro-less scenario and effectively filtering measurement noise to provide a smooth attitude estimate, following the rigorous theoretical framework detailed by Markley and Crassidis [4].

The filter is implemented using a multiplicative error formulation, which is preferred over standard additive corrections because it naturally preserves the quaternion unit-norm constraint during the update step, ensuring the geometric validity of the attitude without requiring brute-force normalization.

In accordance with the same reference, the Kalman update stage employs a minimal three-component representation for the attitude error  $\delta\alpha$ . Consequently, the filter operates on a reduced  $6 \times 1$  error state vector defined as  $\delta\mathbf{x} = [\delta\alpha^T, \delta\omega^T]^T$ . This design avoids the covariance rank-deficiency issues inherent to the four-component quaternion redundancy and ensures a strictly non-singular  $6 \times 6$  error covariance matrix.

**Filter Tuning and Covariance Matrices** The performance of the MEKF relies heavily on the proper tuning of the covariance matrices  $Q$ ,  $R$ , and  $P$ . The selection of these parameters was driven by the relative reliability of the sensors versus the process model.

- **Process Noise Covariance ( $Q$ ):** This matrix models the uncertainty in the system dynamics (e.g., disturbance torques, inertia uncertainties). In this design, the elements of  $Q$  were tuned to be relatively high compared to the star sensor noise. This tuning choice reflects a design philosophy where the filter places greater trust in the high-precision measurements from the Star Sensor rather than relying solely on the open-loop integration of the dynamic model, which is prone to drift over time.
- **Measurement Noise Covariance ( $R$ ):** This matrix characterizes the noise levels of the sensors. The values were assigned based on the sensor datasheets and simulation analysis. The sub-matrix corresponding to the Star Sensor was set with low variance values, reflecting its high accuracy. Conversely, the Magnetometer sub-matrix was tuned with higher variance values, accounting for its inherent sensor noise and sensitivity to electromagnetic disturbances.
- **Error Covariance Matrix ( $P$ ):** The initial value of  $P$  was tuned to balance the convergence speed against the risk of initial overshoot. A properly initialized  $P$  ensures that the Kalman gain settles rapidly, allowing the filter to recover the correct attitude and rate estimates shortly after initialization.

**Estimation Results** The effectiveness of the filtering stage is demonstrated by comparing the raw attitude measurements with the MEKF estimates. As illustrated in Figure 9a, the raw signal exhibits significant high-frequency noise. The MEKF successfully attenuates this noise, providing a smooth and continuous estimate of the state.

This noise reduction is critical for the stability of the *Pointing Control* loop. Since the attitude control law (PD) relies on a derivative term ( $K_d \cdot \dot{\mathbf{e}}$ ), any high-frequency noise in the attitude estimate would be amplified by the derivative action. This would result in "jittery" control commands, causing unnecessary stress on the actuators, higher power

consumption, and potential saturation. The clean estimate provided by the MEKF allows the controller to operate smoothly, reacting only to genuine dynamic movements rather than sensor noise.

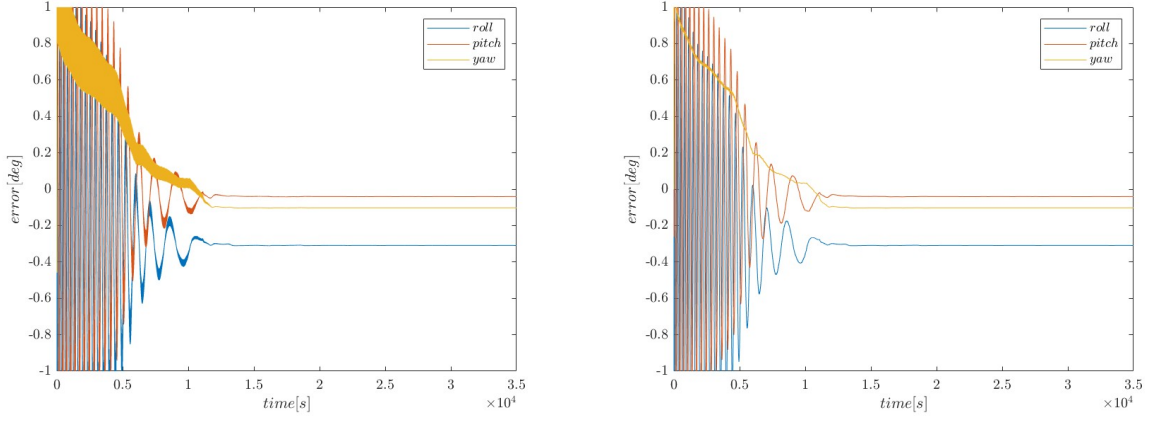


Figure 9: Attitude estimation

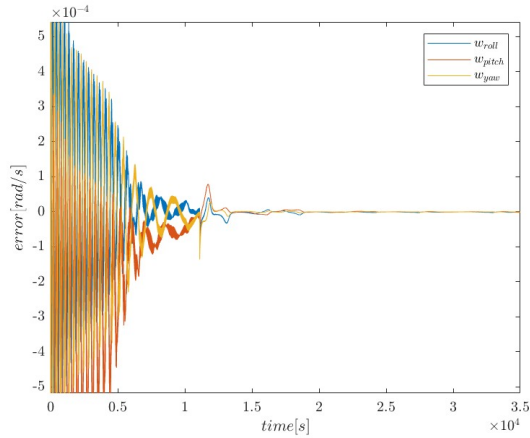


Figure 10: Angular Velocities Estimation Error

A particularly significant achievement of the proposed estimation architecture is the high fidelity of the angular velocity reconstruction, despite the complete absence of physical rate gyroscopes. As evidenced by the estimation error plot in Figure 10, the MEKF successfully acts as a "virtual gyroscope." The estimation error remains consistently bounded within the order of  $10^{-4}$  rad/s, converging toward zero as the filter reaches steady state. This result confirms that the high precision of the Star Sensor updates, combined with the accurate propagation of Euler's dynamical equations within the filter, allows for the angular rates to be rendered fully observable with a level of precision comparable to hardware-based solutions.

## 7 Controller Design

The attitude control system is divided into two distinct operational modes: the *Detumbling Mode*, responsible for stabilizing the satellite after deployment, and the *Pointing*

*Mode*, responsible for precise inertial alignment. The design strategies for these two controllers are detailed below.

The primary objective of the detumbling phase is to dissipate the initial kinetic energy of the satellite and reduce the angular body rates to a safe threshold for the reaction wheels to take over. This phase relies exclusively on magnetic actuation via magnetorquers.

The control law implemented is the *B-Dot* algorithm. The commanded magnetic dipole  $\mathbf{m}_{req}$  and the initial theoretical estimate for the gain  $K_{bdot}$  (based on the sizing formula by Markley and Crassidis [4]) are defined as:

$$\mathbf{m}_{req} = -K_{bdot} \frac{\dot{\mathbf{B}}}{\|\mathbf{B}\|}, \quad \text{with} \quad K_{bdot} = \frac{4\pi}{T_{orb}} (1 + \sin \xi_m) J_{\min} \quad (6)$$

where  $\mathbf{B}$  is the measured magnetic field,  $T_{orb}$  is the orbital period,  $J_{\min}$  is the spacecraft minimum principal moment of inertia, and  $\xi_m$  represents the minimum angle between the geomagnetic field vector and the orbit normal. Starting from this analytical baseline, the final gain value was fine-tuned through extensive numerical simulations to maximize dissipation efficiency given the specific orbital parameters and actuator saturation limits.

A critical aspect of the implementation is the derivation of the signal  $\dot{\mathbf{B}}$ . Direct numerical differentiation of the magnetometer measurements would amplify sensor noise, resulting in chattering. To address this, a derivative filter with a low-pass component was designed:

$$H(s) = \frac{s}{\tau s + 1} \quad (7)$$

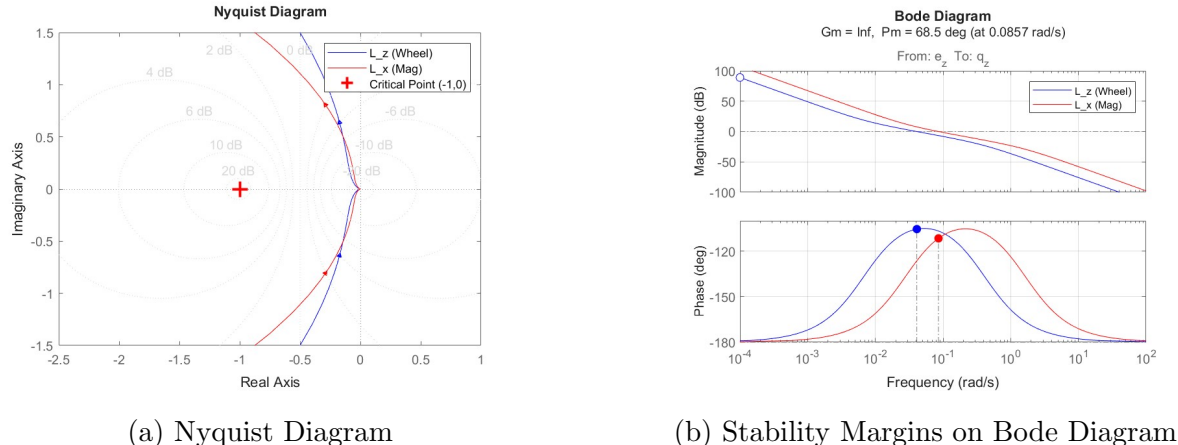
where  $\tau$  is the time constant of the filter. This approach allows for the extraction of the derivative component necessary for the B-Dot law while simultaneously filtering out high-frequency noise, ensuring a clean dipole command for the actuators.

## 7.1 Pointing Control

The pointing controller is designed to maintain a precise inertial attitude. The design process began in the frequency domain, relying on the linearization of the satellite's rotational dynamics. This linear approach is justified by the operational conditions: the controller is activated only after the detumbling phase, ensuring that initial angular rates are low, and the target is inertial pointing, implying small deviations from the equilibrium point.

The stability of the control loop was rigorously assessed using the **Nyquist stability criterion**. The Nyquist diagram was analyzed to verify that the open-loop frequency response did not encircle the critical point  $(-1, j0)$ , thereby confirming the stability of the closed-loop system. Complementing this analysis, the **Bode plots** were utilized to quantify the system's robustness. The **Gain Margin (GM)** and **Phase Margin (PM)** were evaluated to ensure compliance with standard design requirements, providing a necessary safety buffer against modeling uncertainties, unmodeled dynamics, and potential time delays within the loop.

A specific comparison was conducted regarding the bandwidths of the open-loop transfer functions for the two actuation systems. The design deliberately assigns a higher bandwidth to the magnetorquer control loop compared to the reaction wheel loop. This choice is driven by the operational regime of the magnetic actuators: due to their limited torque authority, magnetorquers frequently operate in saturation, effectively behaving as "bang-bang" controllers. A higher bandwidth is therefore necessary to accommodate the

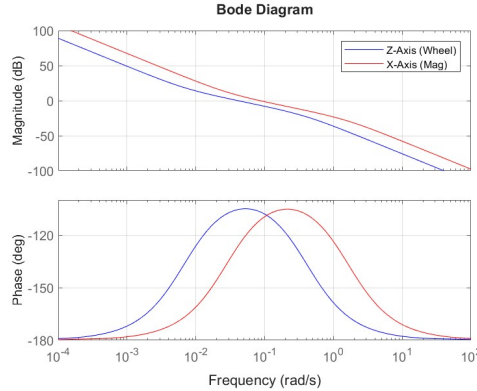


(a) Nyquist Diagram

(b) Stability Margins on Bode Diagram

Figure 11: Controller Performance Analysis

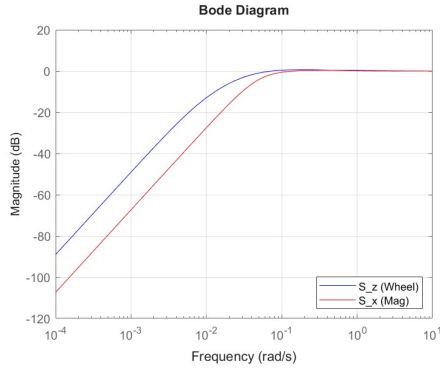
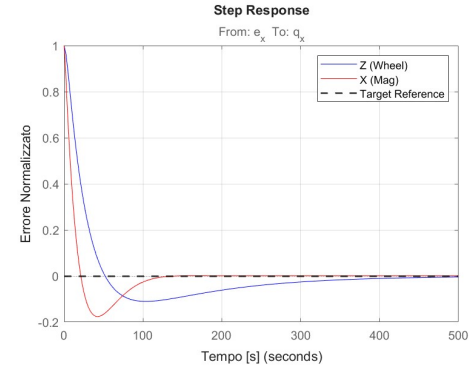
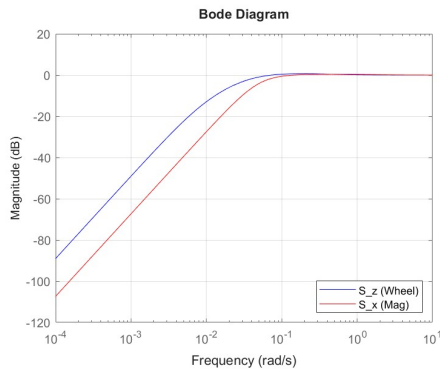
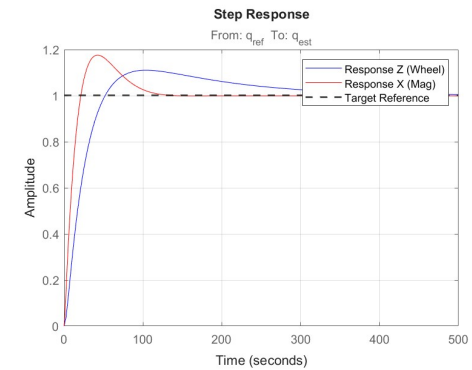
faster dynamics associated with this saturated switching behavior, maximizing their responsiveness when full control authority is demanded. Furthermore, as illustrated in the frequency response plots, the controller shaping achieves a dual attenuation objective: significant magnitude attenuation is enforced at low frequencies to maximize disturbance rejection, while a steep roll-off is implemented at high frequencies to suppress sensor noise effectively.

Figure 12:  $L(s)$  Bandwidth comparison

The controller performance have been validated by analyzing the frequency response of the fundamental system transfer functions. Specifically, the **Loop Transfer Function**  $L(s)$  was examined to assess the stability margins, while the **Sensitivity Function**  $S(s)$  was evaluated to determine the system's disturbance rejection capabilities. Furthermore, the analysis of the **Complementary Sensitivity**  $T(s)$  provided insights into reference tracking performance and sensor noise attenuation. Finally, the **Control Effort**  $Q(s)$  was monitored to ensure that the requested torque remained within the linear operating region of the actuators, avoiding saturation during nominal operations.

Following the theoretical linear design, the controller was implemented and tested within the non-linear Simulink environment. This high-fidelity simulation highlighted the impact of non-linearities, sensor noise, and environmental disturbances. Consequently, a secondary fine-tuning phase was required.

Specifically, the proportional gains ( $K_p$ ) were lowered compared to the theoretical values derived from the linear design. This adjustment was necessary to mitigate actuator

(a)  $S(s)$  Robustness(b)  $S(s)$  PerformanceFigure 13: Closed Loop Analysis - Sensitivity Function  $S(s)$ (a)  $T(s)$  Robustness(b)  $T(s)$  PerformanceFigure 14: Closed Loop Analysis - Complementary Sensitivity Function  $T(s)$ 

saturation and prevent aggressive control spikes, particularly during the *handover* phase (transition from detumbling to pointing). In this transient phase, the controller detects a large initial attitude error; a softer proportional action ensures a smooth convergence, avoiding "bang-bang" behavior in the reaction wheels and reducing stress on the hardware.

## 8 Actuators

The attitude control authority is provided by a hybrid actuation architecture comprising \*\*three orthogonal Magnetorquers (MTQs)\*\* and a single \*\*Reaction Wheel (RW)\*\* aligned with the body Z-axis. This specific configuration has been selected to optimize the power-to-performance ratio and to address the specific controllability requirements of the mission phases.

**Magnetic Actuators (Coarse Control)** The three magnetorquers represent the primary actuation source for momentum management and coarse attitude control. Arranged symmetrically along the principal axes, they are capable of generating control torques by the interaction of their intrinsic magnetic dipole with the Earth's geomagnetic field. ( $\tau_{mag} = \mathbf{m} \times \mathbf{B}$ ) During the Detumbling Phase, the magnetorquers operate as the sole active actuators. To maximize the kinetic energy dissipation rate, they are driven

to their saturation limits (Bang-Bang or high-gain B-Dot logic). This strategy ensures a rapid reduction of the initial tumbling rates without engaging the reaction wheel, thereby protecting the mechanical assembly from saturation and excessive gyroscopic stress during high-rate rotations.

**Reaction Wheel (Fine Pointing)** The single Reaction Wheel is mounted along the body Z-axis ( $b_3$ ), coaxial with the Star Tracker, and is activated exclusively during the Pointing Phase. This configuration ensures full control authority around the optical axis, effectively compensating for the magnetic underactuation singularity that occurs when the geomagnetic vector aligns with the boresight. Crucially, the simulation model reintroduces the actuator's physical non-linearities, intentionally neglected during the linearized controller synthesis, to rigorously validate the inertial pointing capabilities under realistic hardware constraints

**Hardware Selection** The actuator selection process is based on the technical specifications provided by the manufacturers for the Mini-Satellite class, as shown in the table below.

Actuator Type	Selected Model	Key Characteristics
Reaction Wheel (x1)	Bradford W18 [2]	<ul style="list-style-type: none"> <li>• Max Torque: <math>\pm 26.5</math> mNm</li> <li>• Momentum Storage: 18 Nms</li> <li>• Max Op. Speed: 4000 RPM</li> </ul>
Magnetorquers (x3)	ZARM MT30-2 [6]	<ul style="list-style-type: none"> <li>• Max Dipole Moment: <math>30 \text{ Am}^2</math></li> <li>• Linearity Error: &lt; 1%</li> </ul>

Table 4: Actuator Selection and Hardware Specifications

## 9 Simulation Results and Performance Analysis

This section presents the validation of the control system against the mission requirements defined in Section 1.2. The analysis follows the mission timeline, evaluating the detumbling capability first, followed by the fine-pointing performance (APE and RPE), the estimation accuracy, and finally the actuator health status.

### 9.1 Attitude Determination & Control Performance

**Detumbling Performance** The first validation step assesses the capability of the B-Dot controller to stabilize the satellite from the initial tip-off conditions.

To simulate a realistic release scenario, the dynamics were initialized with an angular velocity of  $8 \cdot 10^{-2}$  rad/s ( $\approx 4.6^\circ/\text{s}$ ) applied simultaneously to all three body axes. Figure 15 illustrates the time evolution of the body angular velocity norm.

The simulation confirms that the magnetic controller successfully dissipates the initial kinetic energy, reducing the angular rates below the safety handover threshold of  $5 \cdot 10^{-3}$  rad/s defined in Section 1.2 in approximately 2 orbital periods, a performance well within the maximum allowable duration of 3 orbits.

The near-exponential decay of the angular velocity demonstrates the effectiveness of the selected gain and the correct interaction with the geomagnetic field model.

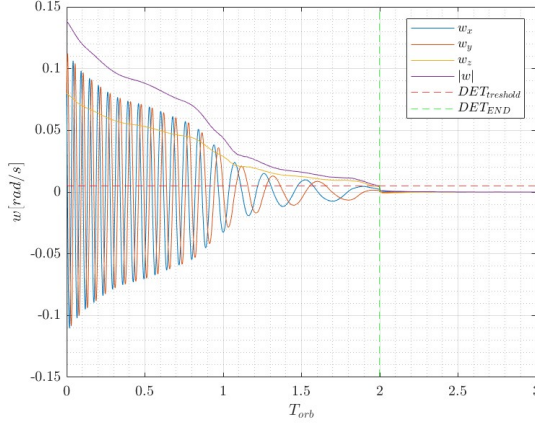


Figure 15: Time evolution of the satellite angular velocity

**Pointing Accuracy and Stability (APE & RPE)** Upon the activation of the fine-pointing mode, the performance is evaluated in terms of accuracy (APE) and stability (RPE).

To provide a comprehensive characterization of the **Absolute Pointing Error (APE)**, the analysis adopts a complementary visualization strategy.

First, the time evolution of the individual matrix elements is plotted to verify element-wise convergence and stability. However, while necessary for formal validation, this nine-component representation does not provide an immediate intuition of the total pointing error. Therefore, the analysis condenses the matrix discrepancy into the most physically meaningful scalar metric: the **Principal Rotation Angle** (or Eigenangle)  $\theta_{err}$ .

This parameter represents the single Euler angle of the error rotation matrix  $\mathbf{A}_{err} = \mathbf{A}_{est}\mathbf{A}_{true}^T$ , effectively quantifying the exact instantaneous angular separation between the estimated and true frames. It is derived from the trace of the error matrix as:

$$\theta_{err} = \arccos\left(\frac{\text{trace}(\mathbf{A}_{est}\mathbf{A}_{true}^T) - 1}{2}\right) \quad (8)$$

The APE represents the accuracy of the payload boresight alignment with the target. Figure 16a shows the scalar angular error between the estimated body attitude and the target attitude. After the initial transient caused by the controller handover, the error converges rapidly and settles below the **5 degree** requirement ( $3\sigma$ ). This confirms that the target star is successfully maintained within the field of view of the Wide-Field Imager.

The stability of the platform is analyzed in Figure 17, which depicts the residual angular velocity (or pointing stability metric) during the imaging phase. The values remain consistently bounded within the **0.05 degree/second** limit. This high stability ensures that the "smearing" effect on the optical sensor is minimized, guaranteeing the required image sharpness for scientific data acquisition.

**Attitude Determination Accuracy** Consistent with the visualization strategy adopted for the pointing performance, the attitude determination error is also quantified using the Principal Rotation Angle (Eigenangle) in Fig.17. This scalar metric effectively condenses the estimation residual into a single value, representing the instantaneous angular distance between the estimated frame and the true reference.

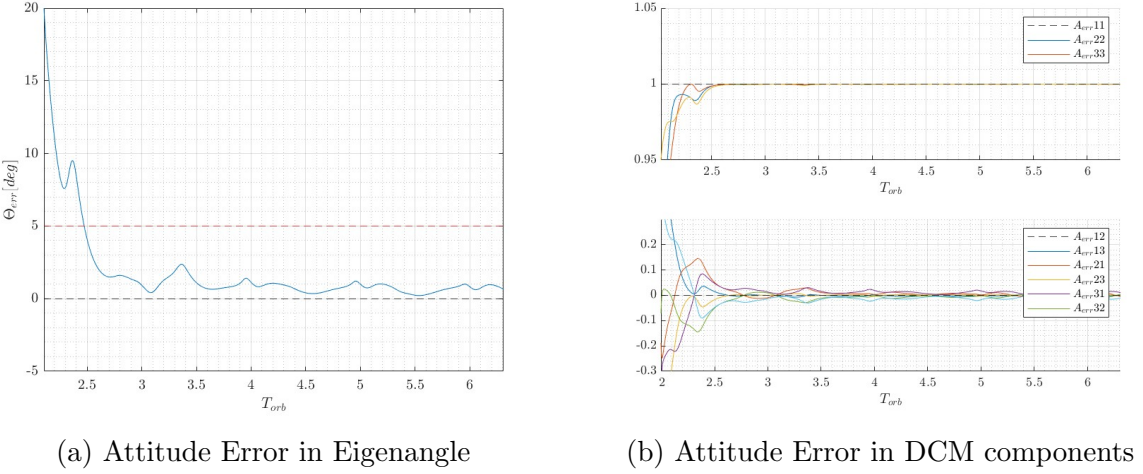


Figure 16: Absolute Pointing Error Analysis

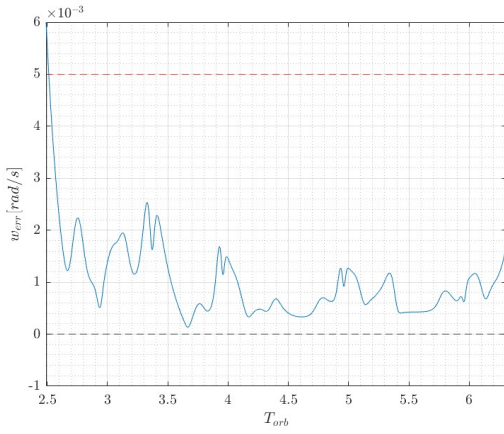


Figure 17: Relative pointing Error

The validity of the control action is strictly dependent on the quality of the estimated state. Figure 18 reports the estimation error, calculated as the difference between the onboard MEKF estimate and the simulation attitude. Despite the gyro-less architecture, the integration of Star Tracker updates allows the determination error to remain well below the **1 degree** threshold. The filter demonstrates robustness against process noise, providing a smooth reference signal to the controller.

It can be observed from Figure 18 that the estimation error, defined as the principal angle between the estimated and true attitude, converges to a steady-state value of approximately  $0.3^\circ$  rather than settling perfectly at zero. This systematic offset can be related to the sensor fusion strategy employed within the MEKF.

The filter architecture is designed to integrate measurements from two distinct sources: the high-precision Star Sensor and the coarser Magnetometer. Although the measurement covariance matrix  $R$  has been tuned to heavily prioritize the optical solution, the Kalman update step inevitably assigns a residual statistical weight to the magnetic readings. Consequently, the lower accuracy of the Magnetometer, combined with local magnetic field disturbances or sensor noise, creates a slight "conflict" with the Star Sensor data. This discordance acts as a persistent drag on the estimate, preventing the filter from converging exclusively on the high-precision optical solution and resulting in the observed

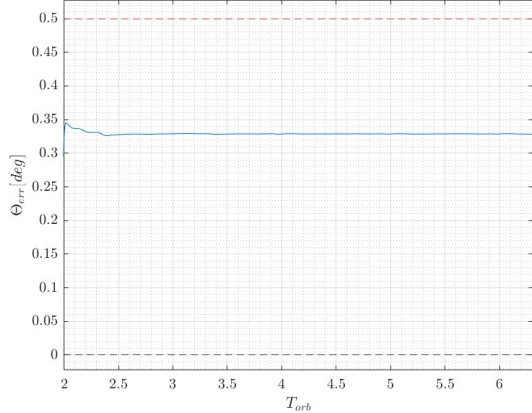


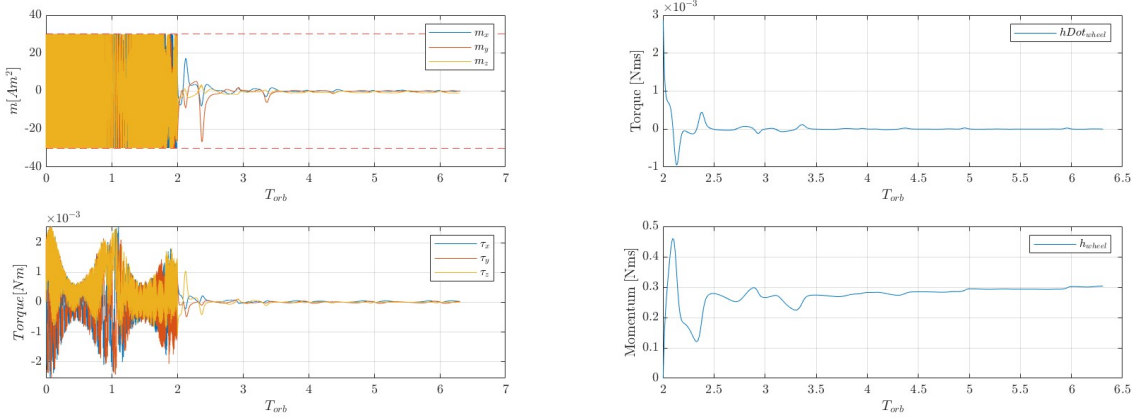
Figure 18: Attitude Determination Error

non-zero steady-state bias.

## 9.2 Actuator Feasibility and Saturation Analysis

The simulation results presented in Figure 19 validate the sizing and selection of the actuators. The magnetorquers (Fig.19a) effectively handle the high-energy dissipation during the detumbling phase, operating in a saturated **Bang-Bang regime** ( $\pm 30 \text{ Am}^2$ ). It is observed that, while the commanded dipole is constant at saturation limits, the resulting torque fluctuates naturally with the local geomagnetic field vector, maximizing the damping effect.

Regarding the Reaction Wheel (Fig.19b), the analysis confirms that the device operates efficiently within a **safe linear region**, far from saturation. The stored momentum stabilizes at approximately 0.3 Nms, utilizing less than 2% of the available capacity (18 Nms). This large margin is a direct consequence of the *hybrid control strategy*, which prevents the wheel from absorbing the initial tumbling angular momentum. Finally, the steady-state control torque drops to the order of  $10^{-3}$  Nm, ensuring stable inertial pointing with minimal mechanical stress on the hardware.



(a) Magnetorquers

(b) Reaction Wheel

Figure 19: Actuator Feasibility and Saturation Analysis

## References

- [1] ACC Clide Space. *Star Sensor - ACC Clide Space*. Available at: <https://www.aacclyde.space/what-we-do/space-products-components/adcs/st200>. 2025.
- [2] Bradford Space. *Reaction Wheels - Bradford Space*. Sito web: <https://www.bradford-space.com/products/rwu> (Accesso: 20-05-2024). 2022.
- [3] European Space Agency. *CHEOPS Spacecraft Overview*. 2025. URL: <https://www.cosmos.esa.int/web/cheops/cheops-spacecraft> (visited on 01/07/2025).
- [4] F. Landis Markley and John L. Crassidis. *Fundamentals of Spacecraft Attitude Determination and Control*. New York, NY: Springer, 2014. ISBN: 978-1-4939-0802-8. DOI: [10.1007/978-1-4939-0802-8](https://doi.org/10.1007/978-1-4939-0802-8).
- [5] NewSpace Systems. *Magnetometers - NewSpace Systems*. Available at: <https://www.newspacesystems.com/magnetometers> (Accesso: 2024-05-20). 2025.
- [6] ZARM Technik. *Magnetic Torquers - ZARM*. Sito web: <https://www.satcatalog.com/component/m2/> (Accesso: 20-05-2024). 2023.